JOURNAL OF GEOPHYSICAL RESEARCH, VOL. 104, NO. B3, PAGES 4795–4809, MARCH 10, 1999

Seismic attenuation tomography of the Tonga-Fiji region using phase pair methods

Erich G. Roth and Douglas A. Wiens

Department of Earth and Planetary Sciences, Washington University
St. Louis, Missouri

Leroy M. Dorman, John Hildebrand, and Spahr C. Webb

Marine Physical Lab, Scripps Institution of Oceanography
University of California, San Diego, La Jolla

Abstract. The anelastic structure of the region surrounding the Tonga slab and Lau back arc spreading center in the southwest Pacific is studied using data from 12 broadband island stations and 30 ocean bottom seismographs. Two differential attenuation methods determine δt^* over the frequency band 0.1 to 3.5 Hz for earthquakes in the Tonga slab. The *S-P* method measures the difference in spectral decay between *P* and *S* waves arriving at the same station. The *P-P* method measures the difference in spectral decay for *P* waves with different paths through the upper mantle. Eight hundred sixty phase pairs are used to invert for two-dimensional $1/Q_\alpha$ structure using a nonnegative least squares algorithm. A grid search method determines the Q_α/Q_β ratio most compatible with both the *S-P* and *P-P* differential measurements. The highest attenuation ($Q_\alpha = 90$) is found within the upper 100 km beneath the active portions of the Lau Basin extending westward to the Lau Ridge. These regions probably delineate the source region for the back arc spreading center magmas, expected to be within the upper 100 km based on petrological considerations. The high attenuation regions also correlate well with zones of low *P* wave velocity determined by regional velocity tomography. Somewhat lower attenuation is found beneath the Fiji Plateau than beneath the Lau Basin. The entire back arc is characterized by a gradual decrease in attenuation to a depth of 300 to 400 km. The slab is imaged as a region of low attenuation ($Q_\alpha > 900$) material. A Q_α/Q_β ratio of 1.75 provides the best fit between the *S-P* and *P-P* data sets upon inversion. Spectral stacking shows no frequency dependence within the frequency band analyzed.

1. Introduction

A great deal of work has been done to investigate the seismic structure of subduction zones and their associated back arc spreading centers. Most of this work has been focused on the seismic velocity structure. However, the anelastic properties of the upper mantle provide important additional constraints on temperature and partial melt production [*Forsyth*, 1992]. In this study we investigate the attenuation structure of the Tonga subduction zone and Lau back arc basin to provide constraints on the distribution of high temperatures and partial melting as a function of location and depth in a subduction zone and back arc basin. The Tonga region, with fast subduction, high seismicity rates, and rapid back arc spreading, offers an ideal location for mapping the attenuation structure of an island arc system.

Global upper mantle attenuation structure has been investigated by a broad range of studies over the past 30 years. Free oscillation data yield estimates of Q_α in the range of 150 [*Anderson and Hart*, 1978a] to 120 [*Sailor and Dziewonski*, 1978] for the upper mantle. Surface wave studies indicate that the upper mantle is divided into an upper layer of low Q with an underlying region where Q increases rapidly with depth. Estimates of the bottom of the low Q region for the average upper mantle have been given at 400 km [*Anderson and Hart*, 1978b], 300 km [*Durek et al.*, 1993], and about 200 km [*Durek and Ekström*, 1996; *Dziewonski and Anderson*, 1981]. Laterally varying models of mantle attenuation can now be constructed from surface wave data [*Bussy et al.*, 1993; *Durek et al.*, 1993; *Romanowicz*, 1995], but the long wavelengths used and focusing effects from velocity heterogeneity limit resolution to features greater than about 3000 km.

Some body wave studies have investigated the attenuation properties of the upper mantle beneath the ocean basins. *Sheehan and Solomon* [1992] mapped lateral variations in attenuation in the North Atlantic using *S-SS* differential measurements and found that the highest attenuation occurred beneath the mid-ocean ridge, with an average Q_β of 65 for the upper 400 km beneath the ridge. *Ding and Grand* [1993] found a Q_β of 70 for the upper 150 km beneath the East Pacific Rise from long-period waveform modeling. *Sipkin and Jordan* [1980] found an average upper mantle Q_α of 150 for ocean basins and *Bhattacharyya et al.* [1996] found $Q_\beta = 112$ ($Q_\alpha \sim 200$) for the upper 400 km globally.

1.1. Tonga/Fiji Region

This study focuses on the attenuation structure in the vicinity of the Tonga subduction zone, a region with a complex tectonic history. Rifting along the Fiji Fracture Zone and the North Fiji Basin (Figure 1) and the change in polarity from west facing subduction along the Vitiaz Trench to east facing subduction along the New Hebrides Trench resulted in the counterclockwise rotation of the main islands of Fiji by 90° over the past 7 m.y. [*Malahoff et al.*, 1982]. In addition, the initiation of spreading along the Lau back arc spreading center has resulted in the rotation of the Tonga arc

Paper number 1998JB900052.
0148-0227/99/1998JB900052$09.00

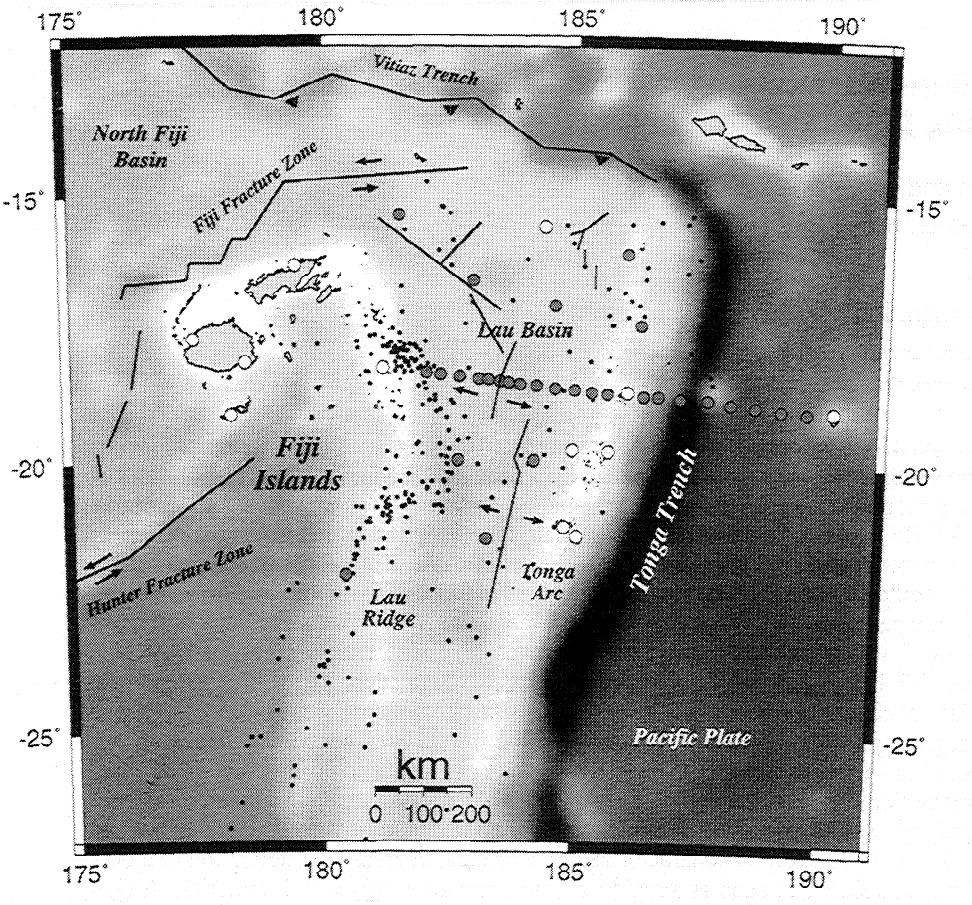

Figure 1. Lambert projection of Southwest Pacific showing location of major tectonic provinces, spreading centers, subduction zones, and transform boundaries. Broadband PASSCAL land stations are shown as larger white circles and OBS stations are shown as small gray circles. All event locations are also plotted as small black dots. Contoured bathymetry is obtained from the National Geophysical Data Center and plotted in shaded gray relief.

away from the Lau Ridge over the last 6 m.y. [*Taylor et al.*, 1996].

Currently the Pacific Plate is being subducted beneath the Tonga arc at a maximum rate of 24 cm/yr [*Bevis et al.*, 1995] near our study area. The Lau Basin contains a series of active back arc spreading centers located between the active volcanic arc and the Lau Ridge. The spreading centers are mostly small laterally offset ridges with spreading rates determined from Global Positioning System (GPS) measurements ranging from 90 mm/yr at 21°S to 160 mm/yr at 16°S . This increase in spreading rate towards the north has given the basin its characteristic V shape. The locations and relative motions of rift zones and spreading centers shown in Figure 1 are taken from *Clarke et al.* [1991], *Auzende et al.* [1994], *Parson and Wright* [1996], *Auzende e. al.* [1995], and [*Taylor et al.*, 1996]. Our study concentrates mainly on the Lau Basin and the lateral and vertical variations in its anelastic structure in the framework of the Fiji Plateau, Tonga subduction zone, and adjacent Pacific Plate.

1.2. Previous Attenuation Models for the Tonga/Fiji Region

Past studies have found a zone of very low Q beneath the active back arc with a sharp transition to high Q towards the volcanic arc, in agreement with global studies of attenuation. Using observations of amplitude and frequency variations in P and S waves to local stations in Fiji and Tonga, *Oliver and Isacks* [1967] assigned an average Q_α of 150 for paths to Fiji and 1000 for paths up the slab to Tonga. *Pn* and *Sn* phases recorded locally have also been used to provide depth constraints on attenuation, yielding the lowest Q_α of 80-150 for depths above 200 km beneath the Lau Basin [*Barazangi and Isacks*, 1971]. *Barazangi et al.* [1974] found high attenuation to depths of 300 km beneath the Fiji Plateau from earthquakes within the intermediate and deep subducted slab. A study using locally recorded P phases by *Bowman* [1988] found $Q_\alpha \sim 240$ above 350 km beneath the back arc and $Q_\alpha \sim 570$ deeper than 350 km, with a Q_α in the slab of over 2000. The most recent studies of the Lau Basin by *Flanagan and Wiens* [1990] and *Flanagan* [1994] using teleseismic long period phase pairs indicate extremely low Q_β of 25 in the uppermost 150 km beneath the active portions of the basin and an increase in Q_β from 35 to 60 towards the west for these depths. For depths of 150-650 km, they found Q_β ranging from 150 to 250.

1.3. Objectives of This Study

The qualitative nature of some of the previous studies as well as the lack of fine-scale ray path coverage indicates the need for a detailed quantitative picture of anelasticity in the upper mantle for this region. In our study, local measurements constrain the fine-scale attenuation structure of the entire Tonga/Fiji region. The phase pair method for studying attenuation has been shown to be an effective way to compute path averaged Q for body waves [*Teng*, 1968; *Flanagan and Wiens*, 1990,1994]. Here we use two

different phase pair methods to measure Q for individual ray paths. We then invert the entire data set for the two-dimensional attenuation structure of the region. The resulting tomographic models of attenuation can be used to correlate regions of anomalous Q with observable tectonic features and possible changes in mantle temperature. Finally, we provide important constraints on the Q_α/Q_β ratio and quantify observable frequency dependence of Q.

Data from an extensive local deployment offers much better resolution than is possible with teleseismic data, as used in previous studies [*Flanagan and Wiens*, 1990]. The station geometry in our study is also an important factor in generating a reliable model of attenuation. Land stations exist on either side of the Lau Basin and, combined with ocean bottom seismographs (OBS) which span the basin and trench, provide excellent spatial resolution. Finally, the use of direct local P and S waves results in a small Fresnel zone, enabling high resolution with lower errors for the inversion. Assuming a frequency of 1.0 Hz, a 600 km deep event will have a Fresnel zone with radius roughly 50 km [*Knapp*, 1991], compared to a Fresnel zone of radius 160 km for teleseismic *sS* phases from deep earthquakes [*Flanagan*, 1994], or over 1000 km for teleseismic *SS* phases at their midpoint [*Shearer*, 1991].

2. Earthquake Data

The data for this study come from two concurrent seismometer deployments in the Tonga/Fiji region (Figure 1). The overall geometry of stations and sources is ideal for obtaining a regional model of Q. The first set of data is taken from 12 three-component broadband Program for Array Seismic Studies of the Continental Lithosphere (PASSCAL) land stations which were operated from December 1993 to December 1995 in Fiji, Tonga, and Niue Island [*Wiens et al.*, 1995]. Nine sites were equipped with Streckeisen STS-2 sensors and three with Guralp CMG3-ESP sensors. Each was controlled by a Reftek 24-bit acquisition system with a GPS clock that recorded data to 1.2 Gbyte disks at sample rates of 20 or 25 samples per second (sps).

The second data set comes from a deployment of 30 ocean bottom seismometers operated from September through December of 1994. Fourteen were the Office of Naval Research (ONR) type [*Jacobson et al.*, 1991] and sixteen were OBSs built by Spahr Webb [*Webb*, 1998]. Each consisted of a three-component Mark Products L-4 1-Hz seismometer and a hydrophone and recorded at 32 Hz. Only the seismic components are used in this study. The close spacing of the OBSs gives us high lateral resolution within the back arc and forearc regions. Over 500 local events were recorded by the OBS array, of which 86 provide adequate signal to noise ratios across the array for this study.

Due to the close proximity of station and source and the predominance of deep earthquakes in the data set, the majority of direct phases arrive at the stations with near vertical incidence. P waves were thus taken from the vertical component and S waves from the transverse or radial components. The events were selected based on location, depth, and magnitude. All events were located within the Tonga slab and range in latitude from 13°S to 26°S. This distribution of events limits the sources to a ~10° longitudinal band from just west of the trench to the deepest events beneath the Lau Ridge. Events range in depth from 50 to 670 km and in M_b from 4.2 to 6.7. We use a total of 268 events yielding 860 phase pair measurements.

3. Data Analysis

The fist step of the data analysis involves the determination of differential attenuation measurements. Using the two types of differential attenuation measurements described below (Figure 2), we compute a δt^* for each phase pair. This quantity is a measure of the difference in the integral, $\int(1/Q)\,dT$, between two phases, where T is the travel time and Q is the seismic quality factor mea-

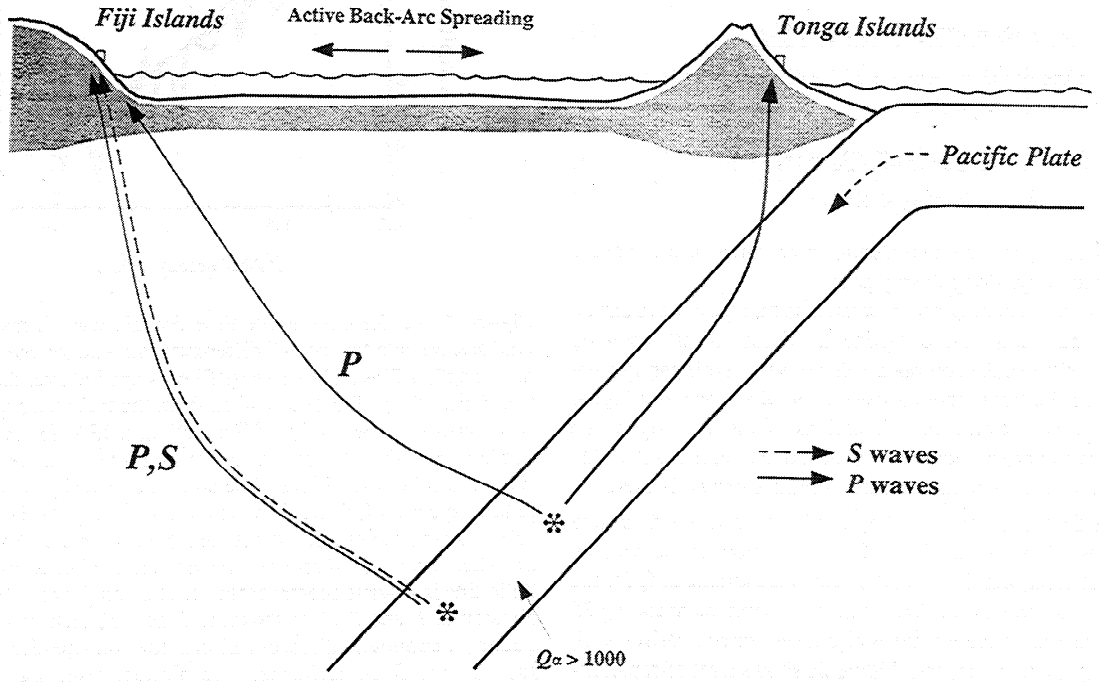

Figure 2. Regional cross section showing idealized rays for *S-P* and P-wave differential attenuation methods. P waves are shown as solid lines, and S waves are shown as dashed lines. The deeper event indicates the propagation of P and S as used with the *S-P* method. The shallower event shows the differential paths taken by P waves used with the P wave method. Both sets of ray paths exist throughout the depth range of 50 to 670 km.

suring energy loss along the two ray paths. The δt^* data are then inverted for the attenuation structure.

3.1. The δt^* Measurements: *S-P* Method

The *S-P* differential attenuation method compares the relative decay of *S* and *P* waves from the same earthquake at a given station. As shown in Figure 2, both phases travel nearly identical paths to the station, providing a single measurement of δt^* for the region spanned by those ray paths. This technique can be used at any local station where both the *P* and *S* waves are observed as distinct arrivals and share a common frequency band of high signal to noise ratio. The spectra of both phases can be expressed by

$$P(\omega) = C_P\, F(\omega)\, I(\omega)\, R(\omega)\, A_P(\omega) \quad (1)$$

$$S(\omega) = C_S\, F(\omega)\, I(\omega)\, R(\omega)\, A_S(\omega), \quad (2)$$

where $F(\omega)$ is the source time function, $I(\omega)$ is the instrument response function, $R(\omega)$ is the crustal response function, $A_P(\omega)$ and $A_S(\omega)$ are the individual attenuation functions for each phase, and C_P and C_S are constants expressing the radiation pattern and geometric spreading. If we assume that the source time function, the instrument response, and the crustal response are the same for both phases, a spectral division yields the differential attenuation operator, $A_{S\text{-}P}(\omega)$ multiplied by a constant that does not affect the calculation,

$$A_{S\text{-}P}(\omega) = (\text{const})\, A_S(\omega)/A_P(\omega). \quad (3)$$

Using the assumption of a frequency independent Q, the attenuation operator of each individual phase can be expressed as

$$A_S(\omega) = \exp(-\omega t^*_S/2) \quad (4)$$

$$A_P(\omega) = \exp(-\omega t^*_P/2) \quad (5)$$

$$t^* = \int dT/Q \quad (6)$$

for a particular phase. The differential attenuation operator is then given as

$$A_{S\text{-}P}(\omega) = \exp[(-\omega/2)(t^*_S - t^*_P)]. \quad (7)$$

If we then define δt^* as a measure of the difference in attenuation between the two phases where

$$\delta t^* = \int_S dT_S/Q_\beta - \int_P dT_P/Q_\alpha = t^*_S - t^*_P \quad (8)$$

$$\delta t^* = -2 \ln[A_{S\text{-}P}(\omega)] / \omega \quad (9)$$

where dT_p and dT_S are the incremental travel times of the *P* and *S* waves, respectively, along the ray path.

The horizontal components are rotated so that the *S* wave can be taken from the transverse component. Values of δt^* obtained from the use of the radial component do not vary significantly from those that use the transverse, however, signal is generally higher for the transverse. Since the orientations of the majority of the OBS instruments are not known, the horizontal component which shows the most coherent and highest amplitude arrival is used.

The time domain signals are then windowed with a 10% cosine taper and a window length of up to 20 s. Variations in the window length do not significantly affect the resultant estimate of Q for the phase pair. A sample of the noise from each component ending 25 s before the arrival of the *P* wave is also taken for comparison with the spectra of the main phases. Figure 3a shows a set of representative waveforms band-pass filtered to match the frequency band used in computing the attenuation operator.

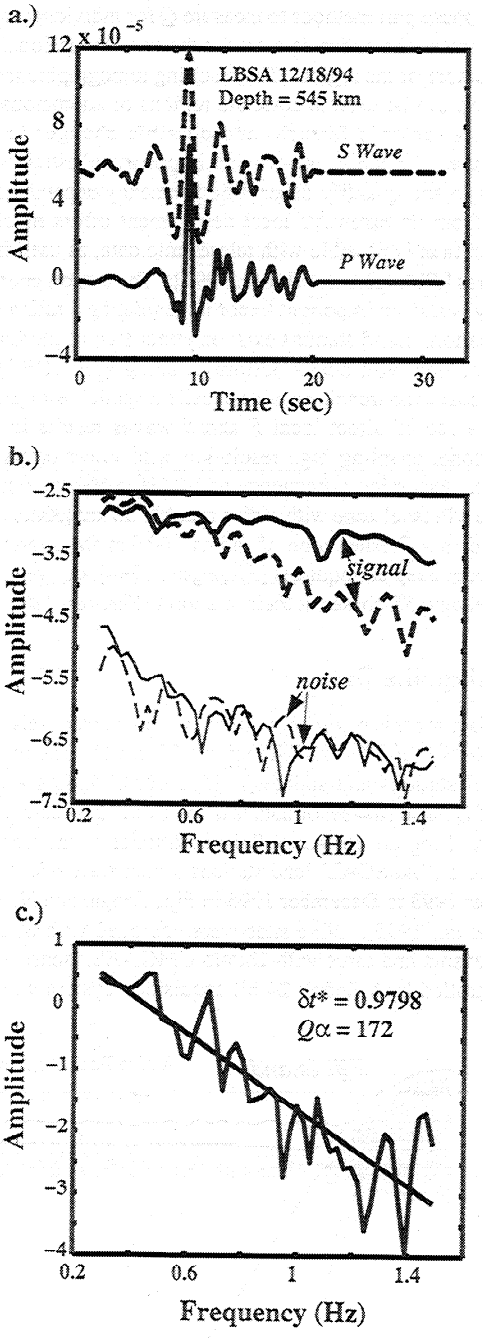

Figure 3. (a) Representative time domain waveforms used with land station data for the *S-P* differential attenuation method. Window length is 20 s and band-pass filter is applied over the range 0.3 to 1.5 Hz. *S* and *P* data are taken from the transverse and vertical components, respectively, of Fiji station, LBSA, for event on December 18, 1994. *S* wave is shown as dashed line and *P* wave is shown as solid line. Travel time picks are made by hand. (b) Amplitude spectra of *S* and *P* waves shown in Figure 3a. Signal is above noise spectra throughout the frequency band. *S* wave spectra taken from transverse component are shown as dashed line. Solid line is *P* wave spectra from vertical component. (c) Spectral division of *P* and *S* wave shown in Figure 3b resulting in the frequency dependent differential attenuation operator. A least squares line fit is performed and plotted, resulting in a δt^* of 0.9798. If a Q_α/Q_β ratio of 1.75 is assumed, a Q_α of 172 can be estimated from δt^*.

We employ a time domain waveform inspection where the useful band of each phase is determined by band-pass filtering over 0.3 Hz intervals beginning at 0.1 Hz . To ensure that we compute δt^* over a frequency range where both P and S waves are well above the noise, only frequency bands where both phases can be clearly seen in the time domain are used. This process yields a useful frequency band for each phase pair. For the S-P phase pair method, the useful band is limited on the high-frequency side by the attenuation of the S wave, and the useful band falls within the range of 0.1 to 2.0 Hz. Phase pairs having useful bands narrower than 1 order of magnitude in frequency are not used.

Using the individual frequency band derived from the above method, the complex amplitude spectra of both phases and both noise samples are taken and the log of the amplitude spectra versus frequency is plotted (Figure 3b). A spectral division then gives the attenuation operator, $A_{S\text{-}P}(\omega)$ (Figure 3c). From (9), we obtain δt^* from the slope of a least squares line fit of $\ln\{\mathrm{mod}[A_{S\text{-}P}(\omega)]\}$ versus frequency (Figure 3c). Fitting the log aids in treating the errors appropriately [*Dorman*, 1968, 1969].

Since the equation for δt^* has the form

$$\delta t^* = T_s/Q_\beta - T_p/Q_\alpha \tag{10}$$

where T_s and T_p are the S and P wave travel times, respectively, an estimate of the ratio between Q_α and Q_β must be assumed to extract an estimate of compressional or shear wave Q. Defining $\gamma = Q_\alpha/Q_\beta$, the equations for Q_α and Q_β take the form

$$Q_\alpha = (\gamma Ts - Tp) / \delta t^*. \tag{11}$$

$$Q_\beta = [T_s - (1/\gamma)T_p] / \delta t^*. \tag{12}$$

If Q and γ are assumed to be independent of frequency over the band used, these formulas are a reliable way to estimate compressional or shear wave Q from measurements of δt^*. In this study we determine the best fitting value of the Q_α/Q_β ratio as part of the inversion.

3.2. The δt* Measurements: *P* Wave Method

Although the S-P method is a reliable way to compute δt^* for a single path, it is limited since ray paths from smaller events passing through regions of extremely high attenuation do not produce clear S waves. To attain higher resolution throughout the region, a second phase pair method using only P waves has been developed.

The P wave method computes differential attenuation between P wave arrivals from the same earthquake at any two stations. We make the same assumptions as in the S-P method, such that a spectral division of both P waves yields the differential attenuation operator,

$$A_{P\text{-}P}(\omega) = (\mathrm{const})\, A_{P1}(\omega)/A_{P2}(\omega) \tag{13}$$

where $A_{P1}(\omega)$ and $A_{P2}(\omega)$ are the amplitude spectra of the P waves at the two stations. The attenuation operator is expressed in a similar format as (7), and δt^* is written as

$$\delta t^* = t^*_{P1} - t^*_{P2} = \int_{P1} (dT_{P1}/Q_{P1}) - \int_{P2} (dT_{P2}/Q_{P2}) \tag{14}$$

where the subscripts $P1$ and $P2$ represent P wave ray paths to the two stations. Thus δt^* again takes the final form of

$$\delta t^* = -2 \ln[A_{P\text{-}P}(\omega)] / \omega. \tag{15}$$

We have exercised considerable care in selecting the waveform pairs for the P wave differential measurements. Back arc stations

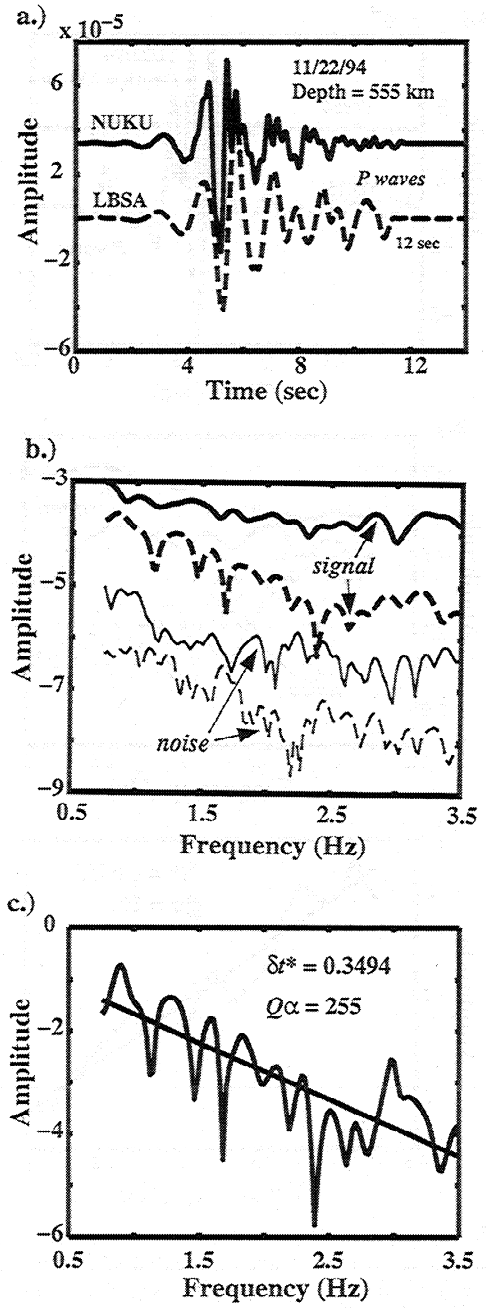

Figure 4. (a) Representative time domain waveforms used with land station data for the P wave differential attenuation method. Window length is 12 s and band-pass filter is applied over the range 0.75 to 3.5 Hz. Both P waves are taken from the vertical component for event on November 22, 1994, recorded at Fiji station, LBSA, and Tonga station, NUKU. LBSA data are shown as dashed line, and NUKU data are shown as solid line. (b) Amplitude spectra of both P waves shown in Figure 4a. Spectra taken from LBSA are shown as dashed line and spectra from NUKU are shown as solid line. (c) Spectral division of both P waves shown in Figure 4b resulting in the differential attenuation operator. A least squares fit to the differential attenuation operator yields a δt^* of 0.3494. If negligible attenuation is assumed for the slab path to station NUKU, a Q_α of 255 can be estimated for the back arc path to LBSA.

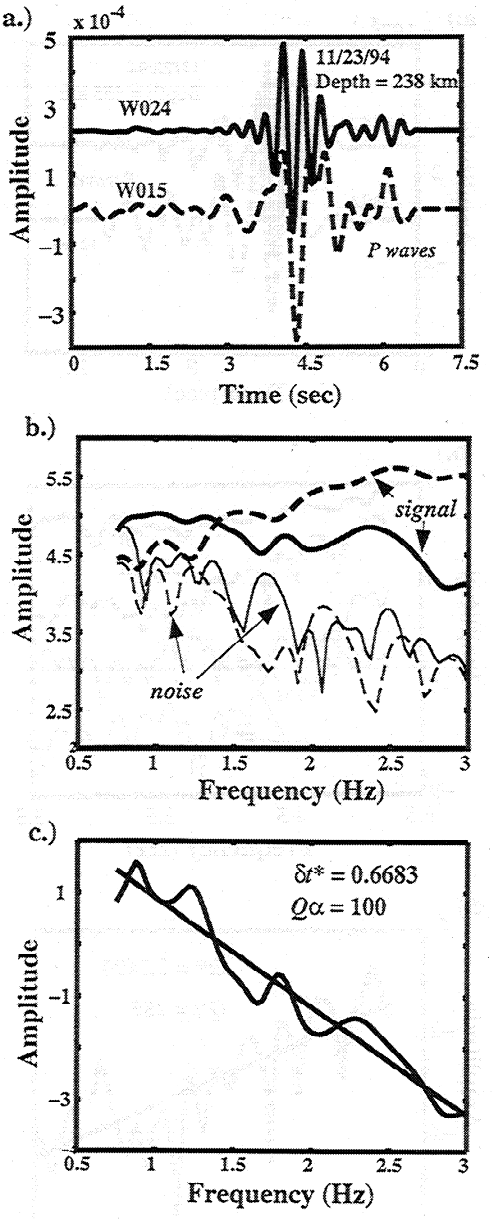

Figure 5. (a) Representative time domain waveforms used with OBS station data for the *P* wave differential attenuation method. Window length is 6 s and bandpass filter is applied over the range 0.75 to 3.0 Hz. Both *P* waves are taken from the vertical component for event on November 23, 1994, recorded at Lau Basin OBS station, W015, and near-trench OBS station, W024. W015 data are shown as dashed line, and W024 data are shown as solid line. (b) Amplitude spectra of both *P* waves shown in Figure 5a. Spectra taken from W015 are shown as dashed line and spectra from W024 is shown as solid line. (c) Spectral division of both *P* waves shown in Figure 5b resulting in the differential attenuation operator. A least squares fit to the differential attenuation operator yields a δt^* of 0.6683. If negligible attenuation is assumed for the slab path to station W024, a Q_α of 100 can be estimated for the back arc path to LBSA. Station W015 shows higher attenuation than any other station in the array and is directly adjacent to the active back arc spreading center.

are generally paired with near-slab stations to avoid phase pairs with highly similar individual t^* values. Land stations are never paired with OBSs due to uncertainties in the compatibility of the instrument responses. Also, since there are two different OBS types, the OBSs are only paired with those of similar type to avoid problems due to the uncertainties in the responses.

Figures 4a and 5a show two representative pairs of *P* waves for the *P* wave method, one from the land stations and one using OBS data. Both *P* waves are filtered over a range of frequency bands between 0.1 and 4.0 Hz to arrive at a suitable band for each phase pair. Stations near the trench contain good signal as high as 4.0 Hz; however, back arc stations sometimes have no *P* wave signal above 2.5 - 3.0 Hz due to high attenuation. The analysis of the windowed data is the same as for the *S-P* method. The complex amplitude of both phases and both noise samples is computed (Figures 4b and 5b). A spectral division is then performed, resulting in the attenuation operator, $A_{P\text{-}P}(\omega)$. Finally, δt^* is computed from the slope of a least squares line fit of $\ln\{\mathrm{mod}[A_{P\text{-}P}(\omega)]\}$ versus frequency (Figures 4c and 5c).

3.3. Error Estimates for δt^* Measurements

Errors in the data are difficult to estimate formally. Individual statistical errors in the measurements of δt^* for both approaches are computed from the standard deviations of the least squares line fit of the attenuation operator. This is only an estimate of how well the derived attenuation operator approximates a line. There is a broad range in these errors from 1.5 to 45%, with small δt^* values having higher percentage errors. More serious systematic errors may result from the effects of crustal structure, source directivity, and the assumption of idealized ray theory paths. The best estimate of the errors in the model probably comes from scatter within data from similar paths. In the tomographic inversion the model uncertainties are computed from the error in fitting the δt^* values.

Rupture directivity has the capability to bias the observed δt^* values. For the *S-P* method, the similarity of the takeoff angle at the source for both rays will reduce the directivity effects on the spectra. The *P* wave method analyzes phase pairs for which the two rays may have much different takeoff angles. In this study we did not use data from the very large events with long rupture durations such as the March 9, 1994, M_w = 7.6 event in order to reduce the effects of directivity. However, some effects of rupture directivity undoubtedly affect the measurements. We assume that the rupture directions will be randomly oriented for events in this study; therefore the rupture effects should cancel out for a large number of events with highly variable ray path geometries. Thus rupture directivity may cause scatter in the individual δt^* observations but is not expected to cause a systematic bias in the attenuation model.

3.4. Trends found in the individual data

It is sometimes useful to estimate a path averaged Q_α value for an individual source station path. This can be done for the *S-P* method by assuming a Q_α/Q_β ratio, and with the differential *P* measurements if we assume that one of the two phases suffers very little attenuation. *S-P* measurements indicate that the subducting Tonga slab shows Q_α of greater than 1000, suggesting that *P* waves recorded near the trench suffer little attenuation. These phases thus provide an estimate of the unattenuated source spectrum, making it possible to estimate Q_α for the path to the attenuated station by dividing its spectra by the unattenuated station. Then the differential δt^* can be interpreted as the t^* for the ray path to the attenuated station, and the average Q for that path calculated from

$$Q_{P1} = T_{P1}/t^*. \tag{16}$$

The individual δt^* measurements corroborate the trends found in the inversion and have good repeatability. There are 678 *P*

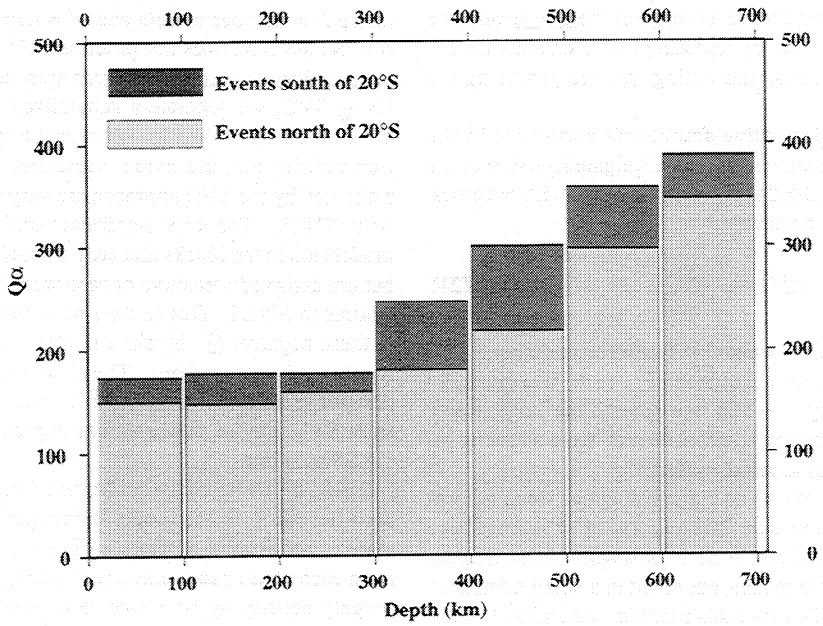

Figure 6. Plot of Q_α versus depth with events binned into north and south regions. Northern events are all events north of 20°S, and southern events fall south of 20°S. All events are also binned into 100 km intervals and averaged. A trend of higher Q in the southern region is apparent. Values obtained for paths confined to the subducted slab are eliminated from this figure since they exhibit very low attenuation and have a small dynamic range over depth and latitude.

wave phase pairs and 182 *S-P* phase pairs. For reasonable assumed values of the Q_α/Q_β ratio (1.5 - 2.25), there is good agreement between the average Q values found by each method in the same region . The average Q_α of paths to stations in the Fiji Plateau from events deeper than 450 km is roughly 370. For shallow events above 150 km, paths to Fiji stations give $Q_\alpha \sim 175$. The OBS stations directly above the active back arc spreading center show the highest attenuation. This area has not been directly sampled by previous studies which used only land stations. For deep events these stations yield an average $Q_\alpha \sim 250$ and shallow events show $Q_\alpha \sim 110$. The average path Q_α for ray paths through the subducted slab to land stations along the volcanic arc and OBSs adjacent to the trench is 3000, although these slab measurements have higher errors due to the flat slope of the attenuation operator. Adjacent to the forearc, attenuation increases rapidly toward the west. Less than 1° away from the arc, the average Q_α falls to 580 for intermediate and deep events, and at 2° it is down to 331.

A strong latitudinal trend is also apparent. Events located in the northern part of the basin (north of 20.0° south latitude) exhibit a roughly 20% lower average Q_α than events in the southern part. Overall attenuation also decreases with depth in all regions. Figure 6 shows values of path Q_α as a function of depth. The data are binned into two groups by latitude as well as into depth bins at every 100 km to show the correlation between attenuation and north-south location as well as depth.

3.5. Inversion of δt^* Data for a 2-D Attenuation Model

We use a tomographic inversion to determine the two dimensional (2-D) structure of the upper mantle from the δt^* measurements. We divide the upper mantle into blocks and invert for Q^{-1} in each block. The observed vector of δt^* values is expressed as a summation of the δt^* within each block along the ray paths,

$$\delta t^*_j = \sum_{i=1}^{\text{nblocks}} (Q^{-1})_i \, \Delta T_{ij} \tag{17}$$

where ΔT_{ij} represents a combination of travel times in a particular block whose form depends on which method of differential attenuation is used.

In order to compute the travel time kernel, ΔT_{ij}, we trace rays through the iaspei91 velocity model. The choice of 1-D velocity models does not have a significant effect on the result. The form of the travel time kernel also changes according to whether we are inverting for Q_α or Q_β. From (11), the travel time kernel for the *S-P* method, inverting for Q_α, takes the form:

$$\Delta T^{S\text{-}P}{}_{ij} = (Q_\alpha/Q_\beta)\, \Delta T^S{}_{ij} - \Delta T^P{}_{ij} \tag{18}$$

where $\Delta T^S{}_{ij}$ and $\Delta T^P{}_{ij}$ are the *S* and *P* wave travel times in each block *i*, for ray path *j*. For the *P-P* method, δt^* is computed as the difference in attenuation along two different paths, the travel time kernel contains contributions from each block that either ray passes through. This leads to a kernel which is the difference in the travel time of the two rays in a particular block:

$$\Delta T^{P\text{-}P}{}_{ij} = \Delta T^{P1}{}_{ij} - \Delta T^{P2}{}_{ij} \tag{19}$$

where $\Delta T^{P1}{}_{ij}$ is the *P* wave travel time for block i along the path to the attenuated stations and $\Delta T^{P2}{}_{ij}$ is the *P* wave travel time along the near-trench path for the same phase pair.

Both methods can be combined in the inversion if a Q_α/Q_β ratio is assumed and if each *P-P* or *S-P* δt^* observation is associated with the correct form of the kernel. The inverse problem, in matrix form, is

$$[\Delta T]_{NM}\,[Q^{-1}]_M = [\delta t^*]_N \tag{20}$$

where M is the number of blocks and N is the number of δt^* data. This form applies for inversions from one to three dimensions and requires no a priori estimates of the attenuation structure. Since

this combined inversion requires an estimate of the Q_α/Q_β ratio, we determine the best fitting ratio by repeating the inversion with different assumed Q_α/Q_β ratios, and noting the one providing the lowest error.

We also use a first derivative smoothing constraint in the inversion. The kernel is augmented with a weighted version of the smoothing matrix S, and the data vector is padded with N zeroes. In matrix form, (20) now becomes

$$\begin{bmatrix} \Delta T \\ wS \end{bmatrix} [Q^{-1}] = \begin{bmatrix} \delta t^* \\ 0 \end{bmatrix} \quad (21)$$

where w is the dimensionless weighting factor for smoothing. The smoothing matrix has values in seconds of -1 to 4. It is generally found that multiplying by $w \sim 100$ will smooth the large poorly constrained variations between adjacent blocks while allowing robust small-scale structures to remain intact.

We invert these equations using either a singular value decomposition (SVD) [*Wilkinson and Reinsch,* 1971] or nonnegative least squares (NNLS). Techniques such as singular value decomposition will generate valid models but result in a small number of blocks with negative Q. To avoid this problem, we employ a standard NNLS technique in all inversions presented here where $\| [T][Q^{-1}] - [\delta t^*] \|$ is minimized subject to the constraint, $[Q^{-1}] \geq 0$ [*Lawson and Hanson*, 1974]. Although the NNLS algorithm yields a model with some extremely high values of Q, the nonnegativity constraint eliminates models that are physically unreal.

The data variance is used as the best estimate of error since it measures how well the model fits the data. This is computed by

$$\sigma_d^2 = [\, \Sigma (\delta t^*_{\text{observed}} - \delta t^*_{\text{predicted}})^2 \,] / [N - M] \quad (22)$$

where N = number of data and M = number of blocks. Since the NNLS algorithm does not produce a G^{-1} (inverted travel time kernel), additional estimates of error must come from another source. Using SVD, we generate a generalized inverse of the kernel and use it to compute data importances (diagonals of the data resolution matrix) and the model variances. The model parameters estimated by the SVD approach are very similar to those generated with NNLS. The only significant differences between the two models are in the blocks that are computed as negative Q^{-1} by SVD but are assigned a positive or zero value by the nonnegativity constraints in NNLS. Due to the smoothing process, blocks adjacent to these negative Q^{-1} blocks will also vary somewhat between the two inversion procedures. The close similarity between solutions derived from the two approaches indicates that error estimates from SVD can be used as close approximations of error for the NNLS solution.

Using SVD, we compute the model covariance matrix, the standard deviation in the model parameters σ_m, the data resolution matrix, and data importances. The sum of the data importances from each phase pair method shows that the solution is determined roughly equally by both data sets. Individual *S-P* data have, on average, a higher data importance, due mainly to their uniqueness of path, and thus contribute as much to the overall solution as the larger total number of *P* wave data. Along with the model covariance matrix, the hitcount and total travel time of rays in each block are used as estimates of how well constrained a particular model parameter is. Blocks having a hitcount of zero are completely determined by the smoothing constraints and are thus eliminated from the models. These blocks do not have any weight in determining values of Q^{-1} in blocks with nonzero hitcount.

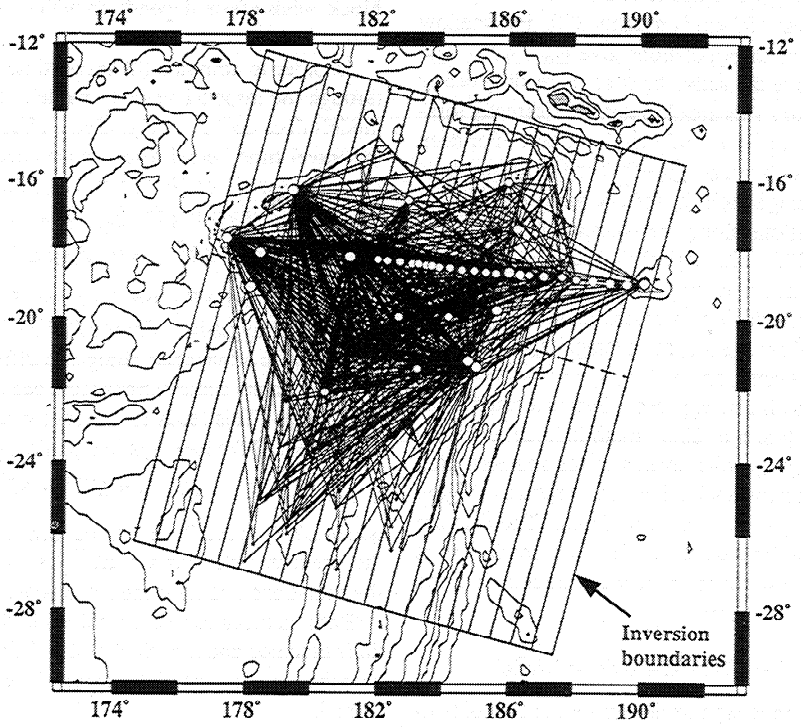

Figure 7. Mercator projection of region covered by this study. Boundaries of inversion are shown projected on the surface. EW boundary used in three-dimensional inversion shown as dashed line. The model consists of 20 blocks in the NNE direction and six vertical blocks perpendicular to the map. The model is rotated 15° from north-south to match the overall strike of the Tonga Trench. Projections of ray paths used in this study are also shown along with event locations. Land stations are shown as large circles and OBS sites are shown as smaller circles.

4. Results

4.1. Model Geometry

In the 2-D inversion we assume that the structure is uniform in the direction parallel to slab strike. In order to obtain blocks which parallel the slab, a coordinate transformation is performed which rotates all station and source coordinates 15° clockwise to match the general strike of the trench near Tonga. The outer boundaries are determined from the land stations on the west and east and by the epicenter locations to the north and south (Figure 7). Block size is determined from the data variance reduction, model covariance, and spatial distribution of event locations. A qualitative measure of the resolution of the models can be attained from a picture of the ray path coverage. As can be seen in Figure 7, the ray paths used in the inversion cover almost the entire area with numerous crossing rays.

The data variance and spatial geometry of sources and receivers are the primary factors influencing the block spacing. The model is broken into 20 longitudinal blocks which span 1390 km, yielding a block interval of 69 km. We invert for the structure through a depth range of 675 km, with a depth interval of 100 km in the upper part of the model and 125 km in the lower part. Inversion with models using smaller block size does not lower the variance significantly and results in many blocks with minimal hitcount and low resolution, whereas a larger block size results in significantly higher variance. For the final image, the attenuation values of each block are assigned to a node at its center, and a bilinear interpolation is used to generate a smooth model. To demonstrate the improved fit of the model to the data, we also compute the variance reduction of the 2-D model with respect to a global layered model of attenuation, QM1 [*Widmer et al.*, 1991]. QM1 has depth spacings which are similar to our model. This results in a 382% variance reduction, indicating that our preferred model is a vast improvement over the most detailed global averages.

4.2. Preferred Model

The tomographic model clearly shows most of the major tectonic features in the region (Plate 1). The slab is a prominent low attenuation feature down to at least 400 km, where its attenuation structure is indistinguishable from the surrounding mantle. Q_α within the slab exceeds 900. The extremely high Q region extends, at shallower depths, westward to the active volcanic arc and eastward slightly past the trench. A particularly abrupt transition from the high Q slab to the low Q back arc basin occurs approximately at the Tonga volcanic front. The thickness of the high Q slab is probably slightly exaggerated in the model due to inaccuracies in the ray paths, which are traced in a 1-D model, and due to the smoothing constraints. The image seems to indicate that the slab flattens out and is oriented horizontally at depths below 450 km, as has also been suggested from velocity tomography [*van der Hilst*, 1995]. However, other regions below 450 km are not well sampled, and the high Q at these depths may simply be characteristic of the average 1-D attenuation structure.

The Lau back arc basin is also prominent as a very high attenuation region. The lowest values in the model ($Q_\alpha = 95$) are found

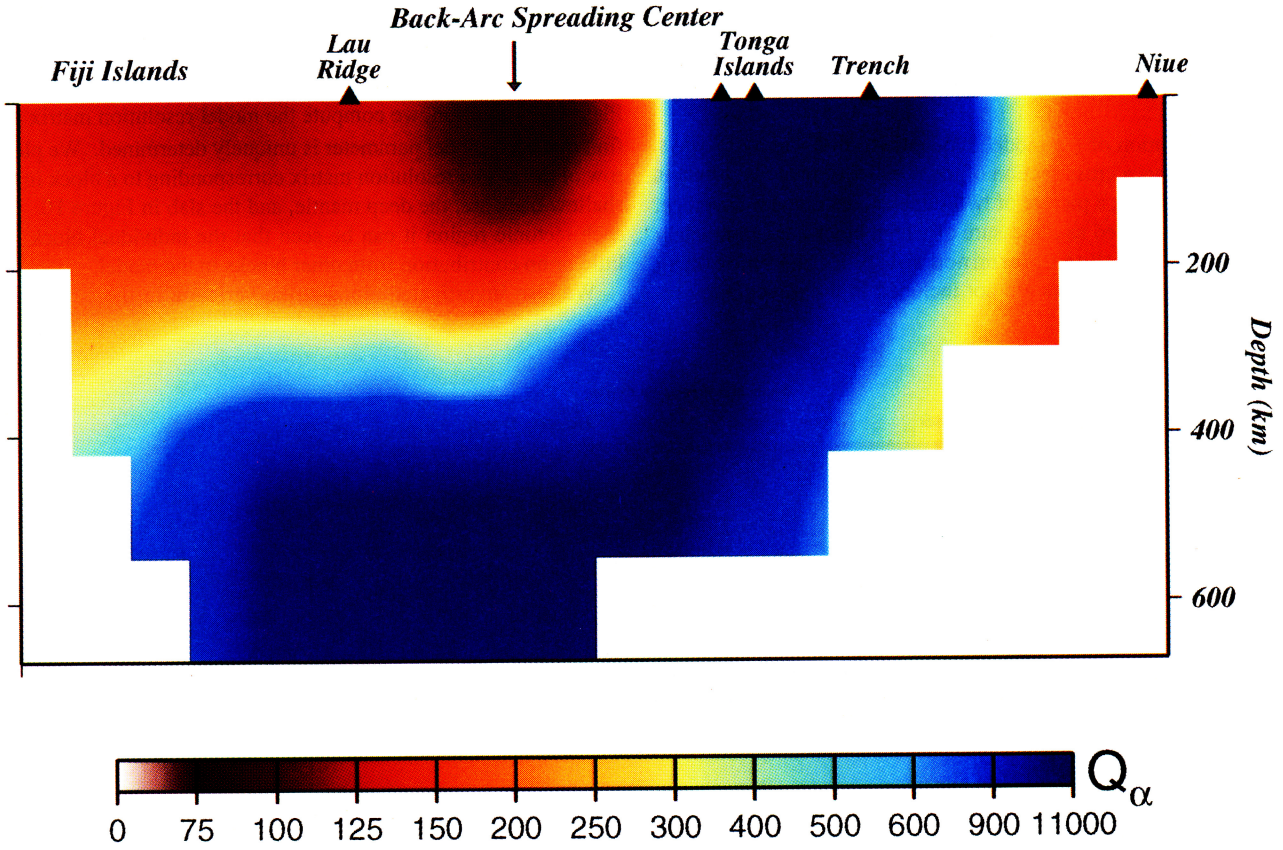

Plate 1. Cross section showing 2-D slice of tomographic model of Q_α. Image is smoothed by a bilinear interpolation scheme. Blocks with zero hitcount are shown as white regions and do not affect the computation of Q within other blocks. Major tectonic features are labeled along the surface. Section is viewed from the south along strike of the Tonga Trench. Horizontal block spacing is 70 km, and vertical block spacing is 100 to 125 km.

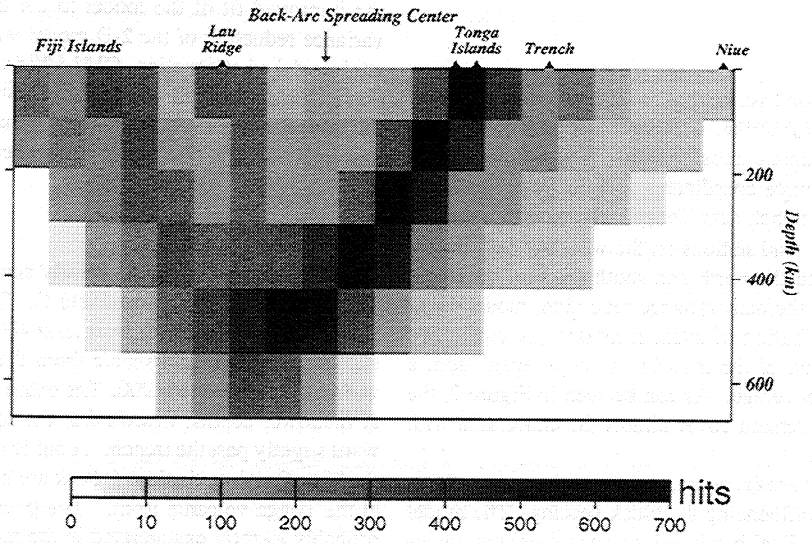

Figure 8. Cross section showing number of rays which travel within each block. View is identical to that shown in Figure 5. Higher hitcounts are plotted as darker shades of gray. Locations of major tectonic features are labeled along top. Blocks with zero hitcount correlate with white blocks in Figure 7.

within the upper 100 km directly beneath and extending somewhat to the west of the Lau back arc spreading center. The attenuation signature of the active back arc extends down to a depth of about 300 km. The Lau Ridge, at the western end of the Lau Basin, also marks the western end of the low-Q back arc. Throughout the Fiji Plateau and Lau Ridge, moderately low values of Q_α (125-170) are found within for the upper 200 km. These values are roughly 70% of those found to the east of the slab beneath the easternmost station.

The resolution of the model is quantified in a variety of ways. Figure 8 shows a cross section of the number of rays that travel in each block, giving a picture of two-dimensional raypath coverage. The hitcount is used as a measure of which blocks are completely unresolved and thus determined solely by the smoothing parameters. Such blocks are not included in the tomography results presented here. The model covariance is also shown as a measure of our resolution. The normalized diagonal elements of the model covariance matrix from the singular value decomposition inversion are plotted at the proper block locations in Figure 9. This figure shows similar features as are shown by the hitcount but also takes into account how well the block is independently resolved by numerous crossing rays. Regions of the model with very high covariance or very low hitcount are not displayed in Plate 1. In addition, we compute the model resolution matrix and find that each model parameter is uniquely determined. We plot a row of the model resolution matrix corresponding to a block in the shallow back arc, the deep mantle, and the slab in Figure 10. For each tectonic region it can be seen that the individual block has little or no contribution from other blocks in the model.

We also investigated along-strike variation in the attenuation

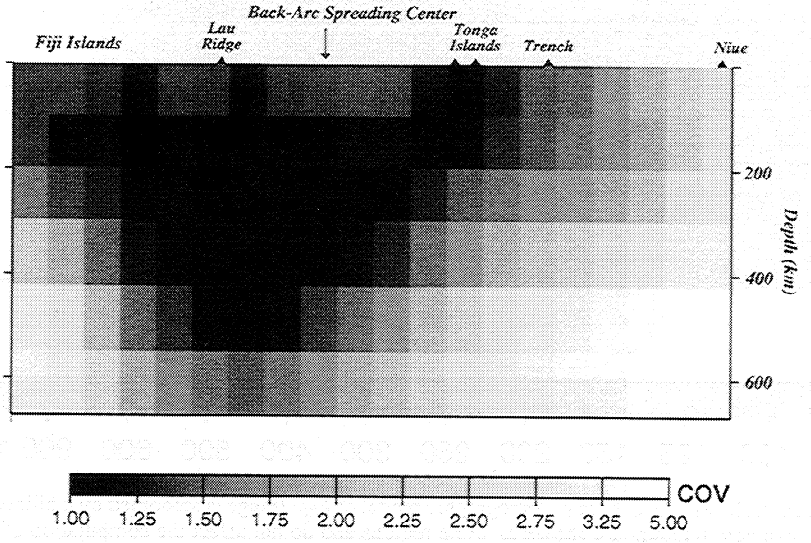

Figure 9. Cross section showing diagonal elements of the model covariance matrix. All values are normalized to 1.0. Each diagonal element corresponds to an individual block and is plotted in that block location. Darker values represent lower covariance and lower error.

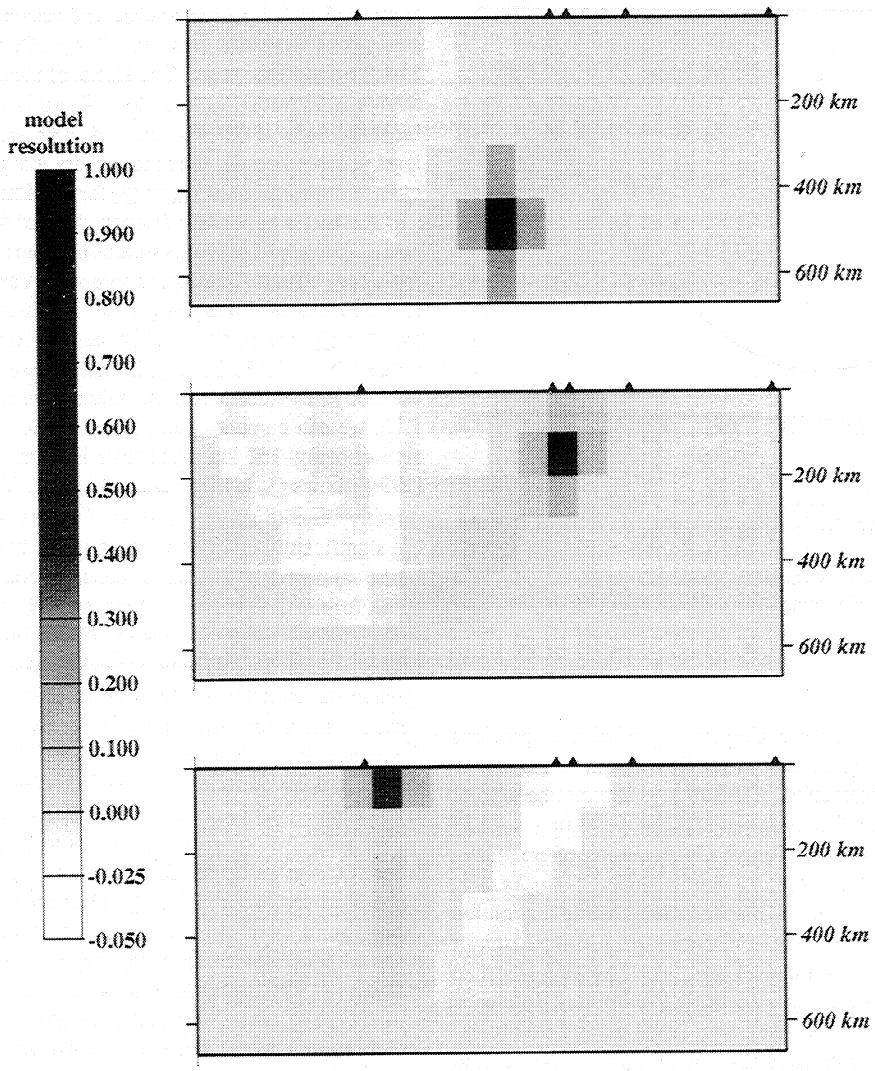

Figure 10. Cross section showing rows of the model resolution matrix corresponding to three blocks within the model. Darker values indicate a higher weight in determining the model parameter for a particular row. The block shown in black represents the diagonal element of the row with the other blocks corresponding to the off-diagonals.

structure by allowing the structure of the northern and southern parts of the model to be separate model parameters. In this "pseudo three-dimensional" model we obtain separate two-dimensional structures for the northern and southern parts of the model, with the dividing line between the northern and southern parts of the model just south of the line of OBSs, as shown by the dashed line in Figure 7. In this case, both the northern and southern structures look very similar to the average structure shown in Plate 1. The primary difference between north and south is in the overall magnitude of the attenuation signatures. Within the upper 300 km of the back arc, the northern region shows Q_α values that are about 10% lower than the southern region, in agreement with the lower individual path averaged Q values found for earthquakes in the northern part of the region (Figure 6). The lower Q values probably result from faster back arc spreading [*Bevis et al.*, 1995; *Taylor et al.*, 1996] and a larger total width of the back arc region in the northern part of the Lau Basin.

4.3. Determination of Q_α/Q_β

The joint inversion of the *S-P* and *P-P* differential attenuation measurements provides constraints on the ratio of Q_α/Q_β. We have taken a forward modeling approach to determine the best fitting Q_α/Q_β ratio for this region. Since the travel time kernel associated with the *S-P* phase pair method is dependent on Q_α/Q_β and the kernel for the *P* wave method is not, if the data sets are internally consistent the ratio determines how well they fit upon simultaneous inversion. To determine the proper ratio, we assume values of Q_α/Q_β in the range of 1.5 to 2.25 and invert for $1/Q_\alpha$ using each value. The data variance is used as a measure of goodness of fit of the inversion and indicates a value of 1.75 for the best fitting Q_α/Q_β. A graph of this ratio versus the variance (Figure 11) shows a minimum error at 1.75.

The ratio of the body wave quality factors can be written in terms of the complex bulk and shear moduli [*Anderson et al.*, 1965]. If it is assumed that there are no losses in pure compression and $V_P = V_S\sqrt{3}$, then $Q_\alpha/Q_\beta = 2.25$. If there is any loss in compression, this ratio will decrease. In a Poisson solid, a ratio less than 2.25 indicates some loss in pure compression. If $V_P > V_S\sqrt{3}$, the ratio can increase past 2.25. Thus there is some trade-off between the Poisson ratio and the ratio between loss in shear and compression in determining the actual ratio between compressional and shear wave Q.

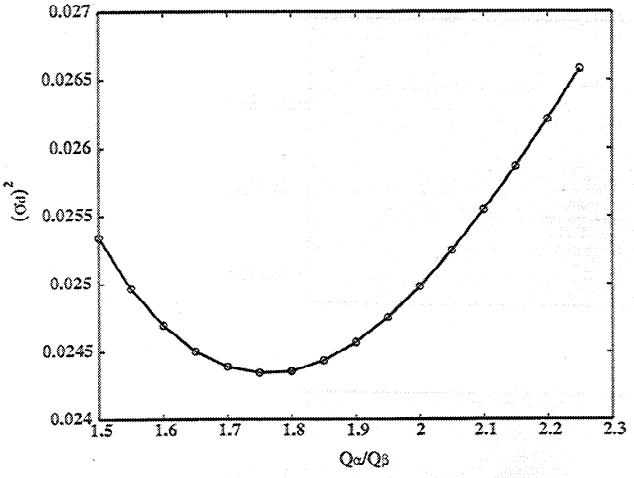

Figure 11. Q_α/Q_β versus data variance for values of 1.5 to 2.25. The inversion is run separately for each value of the ratio at intervals of 0.05. The ratio affects how the *S-P* and *P* wave data sets fit together upon inversion. Minimum variance occurs at Q_α/Q_β = 1.75 and increases continuously for values higher or lower than 1.75.

Our value of 1.75 is a reasonable finding relative to previous work and indicates a loss in bulk of roughly one-third the loss in shear, assuming a Poisson solid. This ratio is similar to a ratio of 1.93 determined by M.P. Flanagan and D.A. Wiens (Attenuation of broadband *P* and *S* waves in Tonga: Observations of frequency dependent *Q*, submitted to *Pure and Applied Geophysics*, 1998)(hereinafter referred to as Flanagan and Wiens (submitted manuscript, 1998)) for the Tonga-Fiji region from comparison of teleseismic *pP - P* and *sS - S* phase pairs. The ratio is lower than the ratio of 2.4 - 2.6 for the upper mantle in Preliminary Reference Earth Model [*Dziewonski and Anderson,* 1981] but is closer to experimental results on granitic rocks, which give a ratio of 1.60 [*Feustal and Young*, 1993]. Thermodynamic results for partial melts indicate a nearly one to one relationship between Q_α and Q_β [*Green and Cooper*, 1992].

4.4. Frequency Dependence of *Q*

Our study assumes both Q_α and Q_β to be constant over the frequency band 0.1 to 4.0 Hz. Stacking of amplitude spectra allows us to substantiate this claim. Since δt^* is determined from the slope of the natural log of the attenuation operator as a function of frequency (9), changes in the slope will yield different estimates of δt^*, and thus *Q*, in different frequency bands. For example, a decrease in the slope of the differential attenuation operator at higher frequencies indicates an increase in *Q* with frequency. One approach used to quantify frequency dependence is to perform each δt^* measurement over a lower and higher frequency band. Doing so for our data set shows no systematic change in slope as a function of frequency for either method.

Since it is possible that this apparent frequency independence is due to scatter in the individual least squares line fits, a more accurate way to investigate frequency dependence is to stack the attenuation operators for each method and look for changes in slope as a function of frequency. Since not all measurements were made over the same frequency band, stacking all the data over one band would generate unreliable results. Instead, the phase pairs from the *S-P* method which were measured over the band 0.3 to 1.5 Hz, and the pairs from the *P* wave method which were measured from 0.75 to 3.5 Hz are stacked and assumed to be representative samples of the entire data set. This yields 90 *S-P* phase pairs and 310 *P* wave phase pairs. The stacks of these amplitude spectra are shown in Figures 12a and 12b. There is no apparent systematic break in slope of either stack, and both are well represented by a least squares line fit. Thus it appears that there is little or no frequency dependence of Q_α or Q_β for the data in this study.

Another way to infer frequency dependence is to compare our results to those of previous studies in same region that use different frequency bands. The most appropriate comparisons can be made to the results of *Flanagan* [1994], in which a tomographic inversion for Q_β was performed for the Lau Basin over the frequency range 0.01 to 0.083 Hz, significantly lower than the band used in our study. By multiplying the values given by *Flanagan* [1994] by 1.75, we can compare them to our model of Q_α. The values are similar below 150 km, but above 150 km the model of *Flanagan* [1994] shows Q_α in the range of 44 to 91. These values, especially directly beneath and to the east of the back arc spreading centers are significantly lower than those found in our model. Variations in the ratio of Q_α/Q_β used to make the comparison would not account for the discrepancy. Flanagan and Wiens (submitted manuscript, 1998) compare long-period and broadband teleseismic *Q* observations from this region and conclude there is significant frequency dependence at frequencies around 0.1 Hz, with longer period observations showing significantly lower apparent *Q*. If the frequency dependence of *Q* occurs mostly at frequencies around 0.1 Hz, it is outside the band used in this study and not inconsistent with the linear slopes of the attenuation operators in Figure 12.

We can also compare our values to those of *Bowman* [1988], where Q_α was computed for individual raypaths over the frequency band 1.0 to 7.6 Hz. These *Q* values are roughly 50% higher than those found from our individual δt^* measurements for similar paths, although this discrepancy may also be due to the fact that the *Bowman* [1988] study had to assume an a priori source spectra model. The *Q* values obtained *Flanagan* [1994], *Bowman* [1988], and this study are all consistent, however, with a general increase in *Q* with frequency. It is therefore possible that minor frequency dependence may exist throughout a wide range of frequencies, but the change in *Q* with frequency may be too small to be detected within the frequency band of an individual study and is only apparent when results from studies of different frequency bands are compared.

5. Interpretation

Ideally, physical or experimental relationships would exist relating attenuation to variables such as temperature, pressure, and the presence of partial melt. However, reliable results of this type are not available at this time. Some studies have attempted to extrapolate from ultrasonic *Q* values obtained in the laboratory to seismic *Q* values. For example, *Sato et al.* [1988, 1989] propose relations between *Q* and the homologous temperature (T_H), which is the ratio of the temperature to the solidus temperature. One difficulty with applying these relations is that they are very sensitive to the actual Q values, which are highly variable from study to study, perhaps due to frequency dependence. For example, the relations for T_H from *Sato et al.* [1989] indicate that for all values of *Q* in our model and in the results of *Bowman* [1988], the temperature is well below the solidus, whereas the back arc regions are at the solidus if the values found by *Flanagan* [1994] for the same region are used. The results of *Sato et al.* [1989] have also been criticized by other experimentalists for having ignored frequency dependence [e.g., *Karato*, 1993]. We conclude that a direct cali-

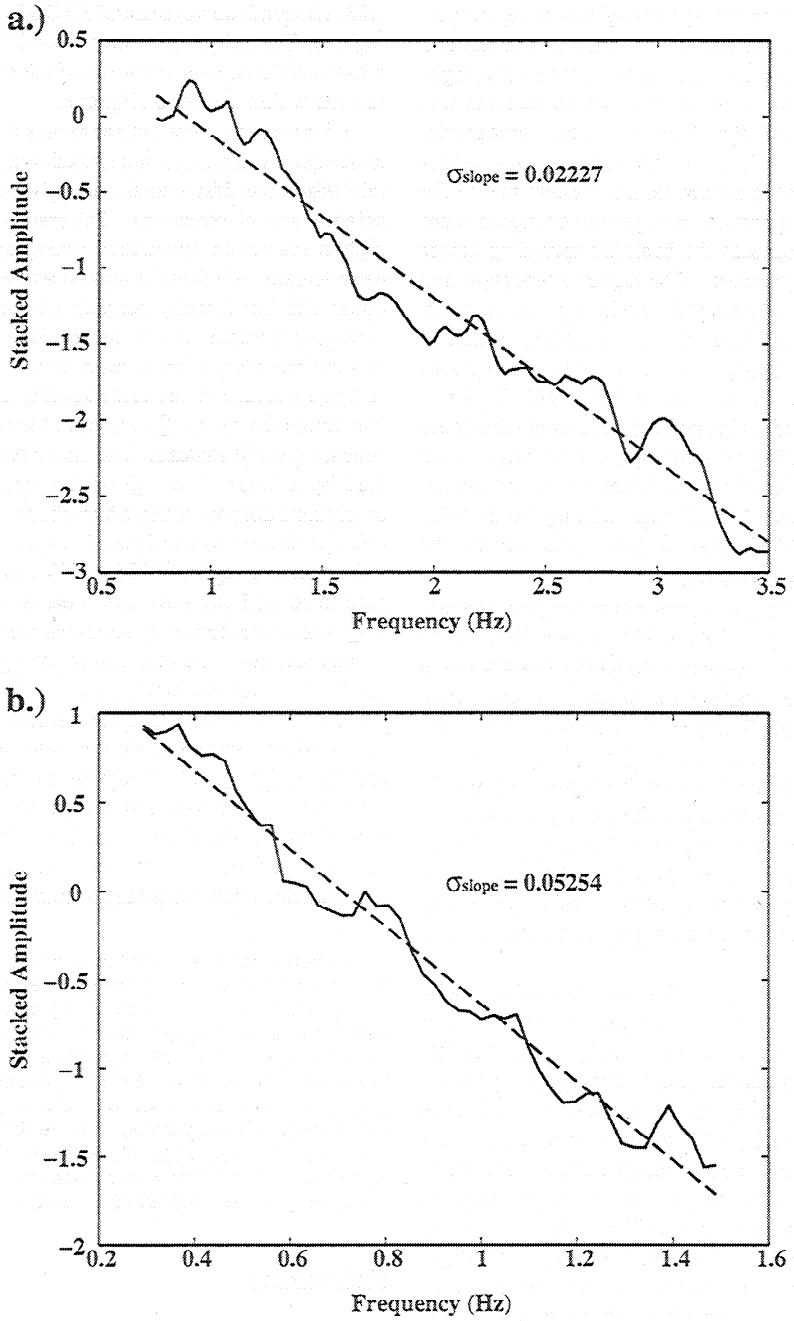

Figure 12. (a) Stack of attenuation operators from *P* wave method computed over the frequency band 0.75 to 3.5 Hz. Linearity of spectra indicates little or no frequency dependence of Q_α for this data set. Least squares fit to the stacked attenuation operators indicates a standard deviation of 0.02227 and is plotted as a dashed line. (b) Stack of attenuation operators from *S-P* method computed over the frequency band 0.3 to 1.5 Hz. Linearity of spectra indicates little or no frequency dependence of Q_α or Q_β for this data set. Least squares fit to the stacked attenuation operators indicates a standard deviation of 0.05254 and is plotted as dashed line.

bration between attenuation and temperature is not reliable at this time and interpret only the relative variations in Q within our model, taking into account other information such as petrological constraints and seismic velocity tomography results.

The attenuation tomography indicates a widespread region of high attenuation in the Lau back arc basin (Plate 1). The region of lowest Q is an area of roughly 200 km horizontally and 100 km vertically directly beneath and to the west of the region of active back arc extension, where we find a Q_α of 95. This region probably corresponds to the primary melt region feeding the Lau back arc spreading center, as petrological and dynamical constraints suggest that the primary melting for formation of oceanic basalts occurs at depths of 20-70 km [*Tanimoto and Stevenson*, 1994; *Shen and Forsyth*, 1995]. Our model is then consistent with a wide zone of primary melting beneath the Lau back arc spreading center.

There is some indication that the eastern part of the Lau basin shows lower attenuation than the western part, as the highest at-

tenuation region extends from the spreading center to the Lau Ridge on the western edge of the basin. This may be partially due to a lack of resolution along the boundary between the high-attenuation basin and the low attenuation slab to the east, but it is also consistent with high-resolution P wave velocity tomography of this region [*Zhao et al.*, 1997], which shows the slowest velocities within the upper 100 km in the central and western part of the basin. This may suggest that primary melt generation region is not symmetrically distributed beneath the back arc spreading center but may be offset toward the west. The higher attenuation and lower velocities in the western part of the basin may be caused by the complex recent tectonics along the Lau spreading center, in which propagating rifts are transferring the zone of active spreading farther toward the west [*Parson and Wright*, 1996; *Taylor et al.*, 1996]. The indication of a wide zone of melt within the upper 100 km asymmetrically distributed with respect to the ridge axis is consistent with recent findings from the Mantle Electromagnetic and Tomography Experiment (MELT) region along the East Pacific Rise [*Forsyth et al.*, 1998], suggesting these features may be characteristic of fast spreading ridges.

A moderately attenuating region surrounds the highest attenuation zone and extends to a depth of about 300 km deep beneath the back arc. This zone extends throughout the back arc basin and is truncated by the Lau Ridge, where the attenuation reverts to the values characteristic of the Fiji Platform. This attenuation extends deeper than would be expected for the major melting associated with seafloor spreading in the back arc, so this region may simply delineate temperatures near but not above the melting temperature. One possibility is that this back arc region is flushed with volatiles released from the slab, which would lower the melting temperature [*Nolet*, 1995; *Navrotsky and Bose*, 1995], such that the back arc material would be near the melting temperature throughout this depth range.

The attenuation image produced in this study is similar to seismic velocity images produced by P wave tomography [*van der Hilst*, 1995; *Zhao et al.*, 1997; *Zhou et al.*, 1997], suggesting that velocity and attenuation anomalies result from similar physical phenomenon, most probably temperature, pressure, and existence of partial melt. The *Zhao et al.* [1997] study uses the same experiment data as used in this study and provides the highest resolution. Close similarities exist between the low-velocity region near the active spreading center of *Zhao et al.* [1997] and the area exhibiting the highest attenuation in the present study. One slight discrepancy between the attenuation and velocity models is the region between 300 and 500 km depth beneath the back arc. The model of *Zhao et al.* [1997] shows P wave velocity anomalies adjacent to the slab between 300 and 500 km depth, whereas there is no corresponding low Q region in our model. The most likely reason for these differences is the lower inherent resolution of the attenuation model, but other possibilities exist. The confining pressures at depths below 300 km may be too high to activate diffusion controlled processes which produce seismic energy loss [*Kampfmann and Berckhemer*, 1985].

6. Summary

We have studied the anelastic structure of the Tonga/Fiji region using two different differential phase pair methods. The first method measures the difference in the spectral content of direct locally recorded P and S waves at the same station. The second uses P wave data from two different stations and computes differential attenuation between both paths. We use data from a deployment of 12 land-based PASSCAL stations in conjunction with a 3 month deployment of 30 OBSs in the forearc and back arc regions. The unique geometry of stations and sources allows us to make individual measurements of attenuation in all of the tectonic regions within the Tonga/Fiji area.

We invert for overall attenuation structure using a nonnegative least squares algorithm associated with a smoothing process that minimizes the first spatial derivative, smoothing blocks to their neighbors in all directions. The results of the inversion show the highest resolution attenuation tomography of an active back arc basin to date. We find the highest attenuation ($Q_\alpha = 95$) within the upper 100 km directly beneath and to the west of the actively spreading portions of the Lau Basin. The Lau Ridge marks the western boundary of this area of lowest Q. This area is accurately sampled because of the close spacing of a majority of OBSs in a line across the basin. Q_α values in the range of 140-200 are found beneath the Fiji Plateau. The entire back arc region is characterized by a layer of low Q with a thickness of 200 to 300 km overlying a deeper mantle which shows very little attenuation. The slab can be seen as a tongue of material with Q_α values exceeding 900 down to a depth of 670 km. We also determine the best Q_α/Q_β ratio to be 1.75 and show that there is little frequency dependence of Q within the frequency band that we investigate.

The results of the attenuation tomography correlate well with the P wave velocity tomography results of *Zhao et al.* [1997] for the same region. Although the resolution of the velocity tomography is higher, regions of slow P wave velocity correlate well with regions of low Q. These regions are most likely features associated with high temperatures and partial melting related to back arc spreading and island arc volcanism. The deeper low Q regions in the back arc (100-300 km depth) may also be related to dehydration reactions occurring deep within the slab.

Acknowledgments. Land instruments were provided by the PASSCAL program of the Incorporated Research Institutions in Seismology (IRIS). Field work was carried out by members of this institution along with Mike Bevis, Wayne Crawford, Kitione Draunidalo, Sharon Esher, Tavita Fatai, Paul Friberg, Saimone Helu, and Mark McDonald. We would like to thank Hersh Gilbert, Brian Park-Li, and Rachel Sakata for the majority of the travel time picks. We would also like to acknowledge Patrick Shore, Megan Flanagan, and Keith Koper for their insight and time put into this project. We also thank Michael Wysession for use of his ray tracing algorithms. This research was supported by the National Science Foundation under grants EAR-9219675, OCE-9314446, and EAR-9614502.

References

Anderson, D.L., A. Ben-Manahem, and C.B. Archambeau, Attenuation of seismic energy in the upper mantle, *J. Geophys. Res.*, *70*, 1441-1448, 1965.

Anderson, D.L., and R.S. Hart, Attenuation models of the Earth, *Phys. Earth Planet. Inter.*, *16*, 289-306, 1978a.

Anderson, D.L., and R.S. Hart, Q of the Earth, *J. Geophys. Res.*, *83*, 5869-5882, 1978b.

Auzende, J., B. Pelletier, and Y. Lafoy, Twin active spreading ridges in the North Fiji Basin (southwest Pacific), *Geology*, *22*, 63-66, 1994.

Auzende, J., R.N. Hey, B. Pelletier, D. Rouland, Y. Lafoy, E. Gracia, and P. Huchon, Propagating rift west of the Fiji Archipelago, *J. Geophys. Res.*, *100*, 17,823-17,835, 1995.

Barazangi, M., and B. Isacks, Lateral variations of seismic-wave attenuation in the upper mantle above the inclined earthquake sone of the Tonga island arc: Deep anomaly in the upper mantle, *J. Geophys. Res.*, *76*, 8493-8516, 1971.

Barazangi, M., B. Isacks, J. Dubois, and G. Pascal, Seismic wave attenuation in the upper mantle beneath the southwest Pacific, *Tectonophysics*, *24*, 1-12, 1974.

Bevis, M. et al., Geodetic observations of very rapid convergence and back-arc extension at the Tonga arc, *Nature*, *374*, 249-251, 1995.

Bhattacharyya, J., G. Masters, and P. Shearer, Global lateral variations of

shear wave attenuation in the upper mantle, *J. Geophys. Res., 101*, 22,273-22,289, 1996.

Bowman, J.R., Body wave attenuation in the Tonga subduction zone, *J. Geophys. Res., 93*, 2125-2139, 1988.

Bussy, M., J.P. Montagner, and B. Romanowicz, Tomographic study of upper mantle attenuation in the Pacific Ocean, *Geophys. Res. Lett., 20*, 663-666, 1993.

Clarke, J.E.H., P. Jarvis, R. Price, and L. Kroenke, Tectonic activity and plate boundaries along the northern flank of the Fiji platform, *South Pacific Applied Geoscience Commission (SOPAC) Tech. Rep. 127*, 1991.

Ding, X.Y., and S.P. Grand, Upper mantle Q structure beneath the East Pacific Rise, *J. Geophys. Res., 98*, 1973-1985, 1993.

Dorman, L.M., Anelasticity and the spectra of body waves, *J. Geophys. Res., 73*, 3877-3883, 1968.

Dorman, L.M., Reply to J.-Cl. De Bremaecker on "Anelasticity and the spectra of body waves", *J. Geophys. Res., 74*, 3304-3307, 1969.

Durek, J.J., M.H. Ritzwoller, and J.H. Woodhouse, Constraining upper mantle anelasticity using surface wave amplitude anomalies, *Geophys. J. Int., 114*, 249-272, 1993.

Durek, J.J., and G. Ekstrom, A radial model of anelasticity consistent with long-period surface-wave attenuation, *Bull. Seismol. Soc. Am., 86*, 144-158, 1996.

Dziewonski, A.M., and D.L. Anderson, Preliminary reference Earth model, *Phys. Earth Planet. Inter., 25*, 297-356, 1981.

Feustel, A.J., and R.P. Young, Q determination using the spectral ratio technique at an underground research laboratory in granitic rock (abstract), *Eos Trans. AGU, 74*, (43), Fall Meet. Suppl.,409, 1993.

Flanagan, M.P., Upper mantle attenuation structure beneath back arc basins using differential shear wave measurements, Ph.D. thesis, Washington Univ., St. Louis, Mo., 1994.

Flanagan, M.P., and D.A. Wiens, Attenuation structure beneath the Lau back arc spreading center from teleseismic S phases, *Geophys. Res. Lett., 17*, 2117-2120, 1990.

Flanagan, M.P., and D.A. Wiens, Radial upper mantle attenuation structure of inactive back arc basins from differential shear wave measurements, *J. Geophys. Res., 99*, 15,469-15,485, 1994.

Forsyth, D.W., Geophysical constraints on mantle flow and melt generation beneath mid-ocean ridges, in Mantle Flow and Melt Generation at Mid-Ocean Ridges, *Geophys. Monogr. Ser.*, vol. 71, edited by J.P. Morgan, D.K. Blackman, and J.M. Sintow, pp. 1-65, AGU, Washington, D. C., 1992.

Forsyth, D.W., S.C. Webb, L.M. Dorman, and Y. Shen, Phase velocities of Rayleigh waves in the vicinity of the MELT experiment on the East Pacific Rise, *Nature*, in press, 1998.

Green, D.H. and R.F. Cooper, Seismic attenuation in partially molten silicate systems: P to S ratios for velocity and Q, *Bull. Seismol. Soc. Am.., 24*, 81, 1992.

Jacobson, R.S., L.M. Dorman, G.M. Purdy, A. Schultz, and S.C. Solomon, Ocean bottom seismometer facilities available (abstract), *EOS Trans. AGU, 72*, (46), Fall Meet. Suppl., 506, 1991.

Kampfmann, W., and H. Berckhemer, High temperature experiments on the elastic and anelastic behaviour of magmatic rocks, *Phys. Earth Planet. Inter., 40*, 223-247, 1985.

Karato, S., Importance of anelasticity in the interpretation of seismic tomography, *Geophys. Res. Lett., 20*, 1623-1626, 1993.

Knapp, R.W., Fresnel zones in the light of broadband data, *Geophysics, 56*, 354-359, 1991.

Lawson, C.L., and R.J. Hanson, *Solving Least Squares Problems*, 340 pp., Prentice-Hall, Englewood Cliffs, N. J., 1974.

Malahoff, A., S.R. Hammond., J.J. Naughton, D.L. Keeling, and R.N. Richmond, Geophysical evidence for post-Miocene rotation of the island of Viti Levu, Fiji, and its relationship to the tectonic development of the North Fiji Basin, *Earth Planet. Sci. Lett., 57*, 398-414, 1982.

Navrotsky, A., and K. Bose, Thermodynamic stability of hydrous silicates: Some observations and implications for water in the Earth, Venus, and Mars, in *Volatiles in the Earth and Solar System*, edited by K. Farley, pp. 221-228., Am. Inst. of Phys., New York, 1995.

Nolet, G., Seismic evidence for the occurrence of volatiles below 200 km depth in the Earth, in *Volatiles in the Earth and Solar System*, edited by K. Farley, pp. 22-32, Am. Inst. of Phys., New York, 1995.

Oliver, J., and B. Isacks, Deep earthquake zones, anomalous structures in the upper mantle, and the lithosphere, *J. Geophys. Res., 72*, 4259-4275, 1967.

Parson, L.M., and I.C. Wright, The Lau-Havre-Taupo back-arc basin: A southward-propagating, multi-stage evolution from rifting to spreading, *Tectonophysics, 263*, 1-22, 1996.

Romanowicz, B., A global tomographic model of shear attenuation in the upper mantle, *J. Geophys. Res., 100*, 12,375-12,394, 1995.

Sailor, R.V., and A.M. Dziewonski, Measurement and interpretation of normal mode attenuation, *Geophys. J. R. Astron. Soc., 53*, 559-581, 1978.

Sato, H., I.S. Sacks, E. Takahashi, and C.M. Scarfe, Geotherms in the Pacific Ocean from laboratory and seismic attenuation studies, *Nature, 336*, 154-156, 1988.

Sato, H., I.S. Sacks, T. Murase, G. Muncill, and H. Fukuyama, Qp-melting temperature relation in peridotite at high pressure and temperature: Attenuation mechanism and implications for the mechanical properties of the upper mantle, *J. Geophys. Res., 94*, 10647-10661, 1989.

Shearer, P.M., Constraints on upper mantle discontinuities from observations of long-period reflected and converted phases, *J. Geophys. Res., 96*, 18,147-18,182, 1991.

Sheehan, A.F., and S.C. Solomon, Differential shear wave attenuation and its lateral variation in the North Atlantic region, *J. Geophys. Res., 97*, 15,339-15,350, 1992.

Shen, Y., and D.W. Forsyth, Geochemical constraints on initial and final depths of melting beneath mid-ocean ridges, *J. Geophys. Res., 100*, 2211-2237, 1995.

Sipkin, S.A., and T.H. Jordan, Regional variation of Q_{ScS}, *Bull. Seismol. Soc. Am., 70*, 1071-1102, 1980.

Tanimoto, T., and D.J. Stevenson, Seismic constraints on a model of partial melts under ridge axes, *J. Geophys. Res., 99*, 4549-4558, 1994.

Taylor, B., K. Zellmer, F. Martinez, and A. Goodliffe, Sea-floor spreading in the Lau back-arc basin, *Earth Planet. Sci. Lett., 144*, 35-40, 1996.

Teng, T., Attenuation of body waves and the Q structure of the mantle, *J. Geophys. Res., 73*, 2195-2208, 1968.

van der Hilst, R.D., Complex morphology of subducted lithosphere in the mantle beneath the Tonga trench, *Nature, 374*, 154-157, 1995.

Webb, S.C., Broad band seismology and noise under the ocean, *Rev. Geophys., 36*, 105-142, 1998.

Widmer, R., G. Masters, and F. Gilbert, Spherically symmetric attenuation within the Earth from normal model data, *Geophys. J. Int., 104*, 541-553, 1991.

Wiens, D.A., P.J. Shore, J.J. McGuire, and E.G. Roth, The Southwest Pacific seismic experiment, *IRIS Newsl., 14*, 1-4, 1995.

Wilkinson, J.H., and C. Reinch, *Handbook for Automatic Computation*: Vol. 2, *Linear Algebra*, 439 pp., Springer-Verlag, New York, 1971.

Zhao, D., Y. Xu, D.A. Wiens, L. Dorman, J. Hildebrand, and S. Webb, Depth extent of the Lau back-arc spreading center and its relation the subduction processes, *Science, 278*, 254-257, 1997.

Zhou, H., Mapping of P-wave slab anomalies beneath the Tonga, Kermadec, and New Hebrides arcs, *Phys. Earth Planet. Inter., 61*, 199-229, 1990.

E. G. Roth and D. A. Wiens, Department of Earth and Planetary Sciences, Washington University, St. Louis, MO 63130-4899. (erich@izu.wustl.edu)

L. M. Dorman, J. Hildebrand, and S. C. Webb, Marine Physical Laboratory, Scripps Institution of Oceanography, University of California, San Diego, La Jolla, CA 92093.

(Received April 24, 1998; revised September 23, 1998;
accepted October 1, 1998.)